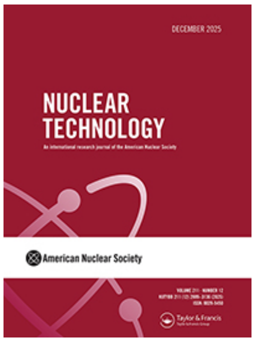

Nuclear Technology

ISSN: 0029-5450 (Print) 1943-7471 (Online) Journal homepage: www.tandfonline.com/journals/unct20

Influence of ATF Cladding Tube Candidates on the Critical Heat Flux in a Vertical Rod Bundle During Flow Boiling of Water at Low Pressure

Nicolas Wefers, Daniel Vlček, Wilson Heiler , Stephan Gabriel & Andreas Class

To cite this article: Nicolas Wefers, Daniel Vlček, Wilson Heiler , Stephan Gabriel & Andreas Class (20 Nov 2025): Influence of ATF Cladding Tube Candidates on the Critical Heat Flux in a Vertical Rod Bundle During Flow Boiling of Water at Low Pressure, Nuclear Technology, DOI: 10.1080/00295450.2025.2536951

To link to this article: https://doi.org/10.1080/00295450.2025.2536951

NUCLEAR TECHNOLOGY
© 2025 The Author(s). Published with license by Taylor & Francis Group, LLC.
DOI: https://doi.org/10.1080/00295450.2025.2536951

Influence of ATF Cladding Tube Candidates on the Critical Heat Flux in a Vertical Rod Bundle During Flow Boiling of Water at Low Pressure

Nicolas Wefers,[a]* Daniel Vlček,[b] Wilson Heiler,[a] Stephan Gabriel,[a] and Andreas Class[a]

[a]*Karlsruhe Institute of Technology, Institute for Thermal Energy Technology and Safety, 76344 Eggenstein-Leopoldshafen, Germany*
[b]*Czech Technical University in Prague, Department of Nuclear Reactors, Faculty of Nuclear Sciences and Physical Engineering, V Holesovickach 2, 180 00 Prague 8, Czech Republic*

Received March 31, 2025
Accepted for Publication July 13, 2025

Abstract — *This paper presents an experimental investigation into the thermohydraulic performance of accident-tolerant fuel cladding materials in a rod bundle configuration under near-atmospheric pressure conditions, representative of simplified light water reactor scenarios. A chromium nitride (CrN)–coated Zircaloy-4 (Zr-4) rod bundle and a fully iron chromium aluminum alloy–clad rod bundle are compared against an uncoated Zr-4 reference, selected for their improved oxidation resistance and reduced hydrogen generation potential. Critical heat flux (CHF) is used as the primary benchmark for evaluating the onset of boiling crisis under steady-state conditions. The influence of alternative cladding materials on surface temperature and maximum heat transfer is assessed at both reduced and elevated operating conditions around a reference point [20 K subcooled mass flux of 200 kg·m^2·s^{-1} at 1400 mbar(a)]. Heating is applied under consecutive steps until the CHF is reached. The test section consists of a directly electrically heated, magnetically compensated five-rod bundle enclosed in a square vertical 43.7 × 43.7-mm^2 flow channel with controlled boundary conditions. Each rod has a 9.5-mm outer diameter, 8.36-mm inner diameter, and 300-mm heated length, additionally with an 8-µm-thick CrN layer. CHF detection is enabled via sight glasses in the flow channel and high-speed imaging, synchronized with a ring buffer and transformer-triggered shutdown, enabling repeated nondestructive tests with various samples. The observed material effects on CHF behavior support the development of mechanistic models and enhance the predictive capabilities of multiphase CFD simulations.*

Keywords — *Experimental investigation, accident-tolerant fuel, rod bundle, critical heat flux, boiling crisis.*

Note — *Some figures may be in color only in the electronic version.*

I. INTRODUCTION

In boiling heat transfer systems, the critical heat flux (CHF) defines the highest achievable heat flux while effectively cooling a heated surface through nucleate boiling. Beyond this critical point, the phenomenon known as departure from nucleate boiling (DNB) occurs. This causes a sudden drop in heat transfer capability, potentially leading to severe component damage within milliseconds.[1] Clearly,

---

*E-mail: nicolas.wefers@kit.edu

the CHF determines essential thermal safety margins, particularly for nuclear reactor fuel cladding.

Zirconium-based alloys have long been the standard choice for fuel cladding in light water reactors (LWRs), primarily due to their advantageous neutron economy and manufacturability. Nevertheless, severe accidents—most notably Fukushima Daiichi—exposed their critical vulnerabilities. Specifically, rapid oxidation in high-temperature steam generates hydrogen, intensifying accident severity.[2] Consequently, researchers globally are pursuing advanced accident-tolerant fuels (ATFs), aiming for better structural and chemical stability under both normal and accident scenarios.[3]

Among these ATF candidates, two prominent strategies have emerged: thin protective surface coatings [like Cr or chromium nitride (CrN) applied via physical vapor deposition] and bulk alloy replacements such as iron chromium aluminum (FeCrAl) alloy. Both approaches substantially enhance oxidation resistance and mitigate hydrogen generation at high temperatures.[4–6] Yet, fully assessing ATF performance requires detailed evaluation of their thermal-hydraulic behavior, especially their CHF characteristics.

Research into CHF began in earnest in the 1960s, producing foundational empirical correlations still widely used today, such as the Groeneveld look-up table (LUT).[7] However, these traditional correlations generally lack sensitivity to evolving surface chemistry and microstructural variations. To address this limitation, researchers developed mechanistic CHF models, linking CHF to physical instabilities like vapor blanket dryout,[8] microlayer depletion,[9] or wettability-dependent regimes.[10] Still, these approaches often require parameters challenging to measure directly, and interlaboratory discrepancies underscore CHF's sensitivity to subtle surface and experimental conditions.[7]

The investigation of CHF in rod bundle configurations remains an active and important research area. For instance, Duan et al.[11] conducted experiments on a 5×5 uniformly heated rod bundle, revealing that CHF increased with higher mass flux and decreased with elevated inlet temperatures, while pressure had a minimal effect under constant inlet temperature conditions. Their findings suggest that using inlet temperature as an independent variable can simplify CHF correlation development. Rao and Pothukuchi[12] focused on low-pressure conditions relevant to small modular reactors and depressurized systems, emphasizing the necessity for accurate CHF predictions to define safe operating heat flux margins in such scenarios. Chen et al.[13] conducted experiments on CHF in a hexagonal seven-rod bundle at low flow and low pressure, revealing that CHF increases with mass flux and pressure but decreases with inlet temperature. They also found that existing correlations underestimated the measured CHF, leading them to propose a new correlation that predicts their data within $\pm 10\%$.

Parallel studies on ATF materials have predominantly involved simplified geometries such as pool boiling or annular flows. Ali et al.[14] investigated the effects of ion irradiation on Cr-coated Zircaloy-4 (Zr-4) surfaces, finding that irradiation altered surface wettability, leading to significant changes in CHF under pool boiling conditions. Kim et al.[6] explored FeCrAl-based claddings, reporting promising CHF performance under annular boiling water reactor–specific conditions. Barrett et al.[15] emphasized the importance of thermal-hydraulic performance evaluation under representative conditions for ATF cladding materials, including rod bundle configurations as relevant geometries to fully assess the performance of ATF claddings.

These studies collectively underscore the importance of evaluating the behavior of CHF in rod bundle configurations to ensure the safe and efficient implementation of ATF materials in nuclear reactors.

Additional insights emerged from the U.S. Nuclear Energy University Program (NEUP), investigating CHF in internally heated annular setups for Cr-coated Zr-4 and FeCrAl tubes. These experiments indicated that while Cr coatings could slightly reduce CHF compared to bare Zr-4, FeCrAl typically matched or marginally improved CHF performance.[16,17] However, because of their annular configuration, direct applicability to reactor rod bundles remains limited.

In related work, Chen et al.[18,19] examined CHF in horizontal annuli using refrigerants (R-134a, R-407C, R-410A), underscoring the significant influence of surface-fluid interactions such as wettability and fluid enthalpy. Their findings clearly support the hypothesis that altering surface characteristics, including wettability and roughness, could meaningfully shift CHF performance, independent of bulk geometry.

Crucially, direct experimental data on CHF for ATF claddings under rod bundle flow boiling conditions remain notably absent, highlighting a clear and important research gap. Addressing this gap, the present study experimentally evaluates the CHF performance of CrN-coated Zr-4 and FeCrAl claddings relative to uncoated Zr-4, using precisely controlled rod bundle flow conditions. Furthermore, a mechanistic CHF model sensitive to material-specific surface properties is developed and validated against experimental results.

I.A. Motivation and Scope of the Present Study

Despite extensive previous research, detailed characterization of CHF for ATF cladding materials in rod bundle configurations remains lacking. To address this critical gap, this study experimentally investigates and compares the CHF values for three materials: bare Zr-4 as a baseline, CrN-coated Zr-4 (coated ATF), and FeCrAl Kanthal APM alloy (bulk ATF).

Experiments were conducted using controlled subcooled flow boiling conditions in a vertical five-rod bundle configuration at near-atmospheric pressures. A combination of optical and thermal diagnostics ensured precise and reliable CHF detection under varying conditions of pressure, mass flux, and subcooling. To robustly quantify experimental uncertainty, 50 repeated measurements were performed at a defined reference point, producing a statistically rigorous data set.

Additionally, to enhance CHF predictions for novel cladding materials, a mechanistic CHF model based on microlayer dryout theory was developed. This model introduces an empirical scaling law for microlayer thickness, incorporating key parameters such as contact angle, critical cavity diameter, specific heat ratio between materials, and thermodynamic quality. The model was calibrated using a single known reference case with Zr-4, thereby enabling predictions for other ATF materials without extensive recalibration.

I.B. Contribution and Outline

The key contributions of this work are threefold:

1. Systematic and statistically robust comparison of CHF values between coated and uncoated claddings specifically in short rod bundle geometries.

2. Quantification of statistically validated differences in CHF behavior between CrN-coated Zr-4 and FeCrAl alloy materials.

3. Quantitative evaluation of the developed mechanistic CHF model, validating its performance against comprehensive experimental data and benchmark Groeneveld LUT predictions.

The remainder of the paper is structured as follows. Section II provides a detailed description of the experimental facility and characterization of test materials. Section III outlines the measurement procedures and uncertainty analysis methods. Section IV introduces the mechanistic CHF model and explains the scaling approach adopted. Section V presents and analyzes the experimental and modeling results. Finally, Secs. VI and VII discuss the implications of these findings for ATF development and future CHF modeling strategies.

II. EXPERIMENTAL SETUP

II.A. Test Facility

All experiments were conducted in the loop Critical heat flux On Smooth and MOdified Surfaces – Low pressure (COSMOS-L) located at the Karlsruhe Institute of Technology. The facility was originally developed for the investigation of surface modifications in annular gap test sections and has since been continuously advanced in both diagnostics and configurational flexibility. More detailed information can be found in Kaiser et al.[20] Today, COSMOS-L enables systematic thermohydraulic studies on advanced cladding materials under controlled low-pressure, subcooled flow boiling conditions. The loop operates in a closed-loop configuration using deionized water and incorporates precise control over flow rate, pressure, and temperature. A schematic overview of the loop is shown in Fig. 1.

Flow control is achieved through a gear pump with a capacity range of 100 to 1000 $\text{kg}\cdot\text{h}^{-1}$, supported by a flow straightener and bypass regulation for fine tuning. The mass flux is monitored using a Coriolis-type flowmeter with a device accuracy of ±0.15%. Pressure regulation is implemented through a pressurized gas bellows tank in combination with an electric heater, allowing accurate adjustment of the absolute system pressure in the range of 1.0 to 2.5 bar(a). The temperature of the working fluid is controlled by an inline heat exchanger connected to a thermostatic bath to achieve the required subcooling, while a thyristor-controlled preheater upstream of the test section ensures a stable inlet temperature.

The heating system is based on a low-voltage, high-current, alternating-current (AC) transformer capable of delivering up to 2.5 kA. Power is transferred via magnetically compensated copper feed lines to minimize inductive noise. Heating power is measured by precision current transformers and a four-quadrant wattmeter. All process variables, i.e., pressure, temperature, flow rate, voltage, and current, are recorded synchronously using a centralized data acquisition system. CHF detection is based on a combination of wall temperature excursions and synchronized optical feedback from high-speed video imaging. A ring-buffered

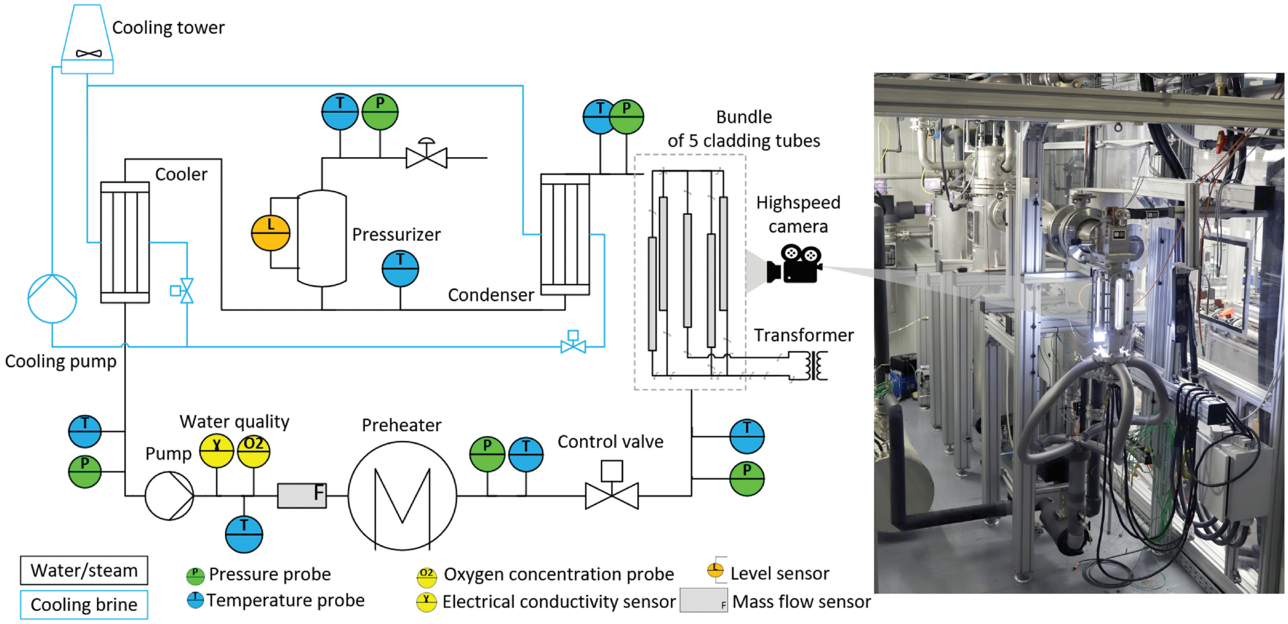

Fig. 1. Schematic overview of the COSMOS-L test loop based on Kaiser et al.[20]

control system captures data 2 s before and 0.5 s after any detected CHF event. An automated shutdown sequence is triggered if abnormal heat flux behavior or incipient dryout is detected.

The COSMOS-L loop is optimized for rapid reconditioning between experiments, enabling repeated CHF measurements without physical modification of the test section. Prior to each test series, a degassing protocol is executed to reduce the dissolved oxygen content in water to 0.6 to 1.2 $\mathrm{mg \cdot l^{-1}}$, minimizing premature nucleation effects.

II.B. Test Section

The test section consists of a vertical five-rod bundle mounted inside a square stainless steel flow housing with optical sight glass windows in the heated region. The rods are arranged in a cross pattern with one central rod and four surrounding rods. The pitch between outer rod surfaces is 20.5 mm, and the center rod has a 14.5-mm pitch to its neighbors. Each rod has an outer diameter of 9.5 mm, a wall thickness of 0.57 mm, and a heated length of 300 mm. Electrical contact is made through solid aluminum end fittings, and heating is applied via direct ohmic resistance from an AC power source.

All rods are geometrically identical and interchangeable with different cladding materials for comparative CHF testing, as shown in Fig. 2. The three cladding variants investigated in this study include commercial uncoated Zr-4, CrN-coated Zr-4 (featuring an 8-µm-thick CrN layer and a 100-nm Ti interlayer deposited via physical vapor deposition), and pure FeCrAl (Kanthal APM) alloy rods. Table I summarizes the material and surface properties that are potentially relevant as indicators of the CHF behavior.

Contact angles were determined using a Krüss K100 tensiometer following the Wilhelmy method in deionized water at 25°C. For each cladding tube, five immersion-withdrawal cycles were performed to capture advancing and receding contact angles, from which the mean value was calculated. The resulting force hysteresis showed negligible variation across cycles, confirming the reliability of the measurement. The averaged contact angle was used as input for the mechanistic CHF model.

Surface roughness measurements were performed using a MarSurf M 310 contact profilometer, with eight sampling locations per specimen—four circumferential and two axial positions. The arithmetic mean roughness R_a and the peak-to-valley roughness R_z were computed along with their respective standard deviations. The observed standard deviations were 0.025 µm for Zr-4, 0.018 µm for CrN-coated Zr-4, and 0.045 µm for FeCrAl. These values were significantly lower than the corresponding mean roughness levels, indicating sufficient surface uniformity for global roughness characterization. Representative profilometry traces revealed that Zr-4 and CrN-coated Zr-4 shared similar microtopography, as shown in Fig. 3, whereas FeCrAl exhibited a distinctly rougher and more heterogeneous surface with deeper valleys and microstructural characteristics.

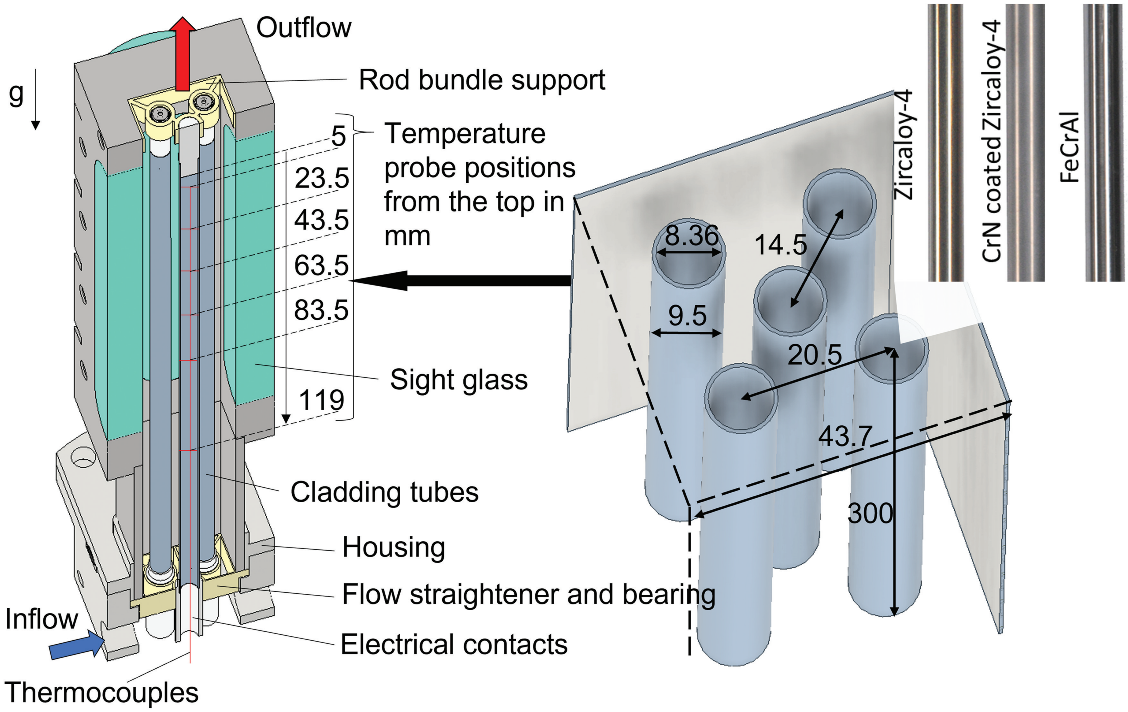

Fig. 2. Schematic of the test section with five-rod bundle inside a square stainless steel flow channel.

III. METHODS

III.A. Measurement Procedure

The experimental determination of the CHF followed a standardized, repeatable protocol based on incremental heating and synchronized detection. Initially, the desired boundary conditions, i.e., mass flux, inlet temperature, and static pressure, were established using the gear pump, throttling valves, heat exchanger, and pressure regulation system. Prior to each measurement, the test loop was degassed by low-power heating until the dissolved oxygen concentration in the water was reduced to between 0.6 and 1.2 $mg \cdot l^{-1}$, thereby minimizing bubble nucleation due to gas pockets.

Heating was applied to the five-rod bundle by direct ohmic heating using AC, with a power increase in discrete steps of approximately 5.6 $kW \cdot m^{-2}$/interval. Each heating level was kept constant for a minimum of 30s to ensure thermal stabilization and avoid premature triggering of CHF due to transient fluctuations. This process was continued until nucleate boiling developed and eventually transitioned to slug flow regimes. As an illustration, the incremental approach to the CHF conditions can be seen in Fig. 4.

TABLE I

Material and Surface Properties of Cladding Tubes as a Reference at Room Temperature

Property	Zr-4	CrN-Coated Zr-4	FeCrAl
Outer diameter (mm)	9.50	9.516	9.50
Inner diameter (mm)	8.36	8.36	8.36
Wall thickness (mm)	0.57	0.578	0.57
Heated length (mm)	300	300	300
R_a (μm)	0.13	0.15	0.25
R_z (μm)	1.34	1.67	3.01
Contact angle (mean) (deg)	85	73	50
Thermal conductivity ($W \cdot m^{-1} \cdot K^{-1}$)	13.4[21]	2.0[22]	11.0[23]
Specific heat ($J \cdot kg^{-1} \cdot K^{-1}$)	281[24]	460[22]	460[23]
Coating thickness (μm)	—	8	—

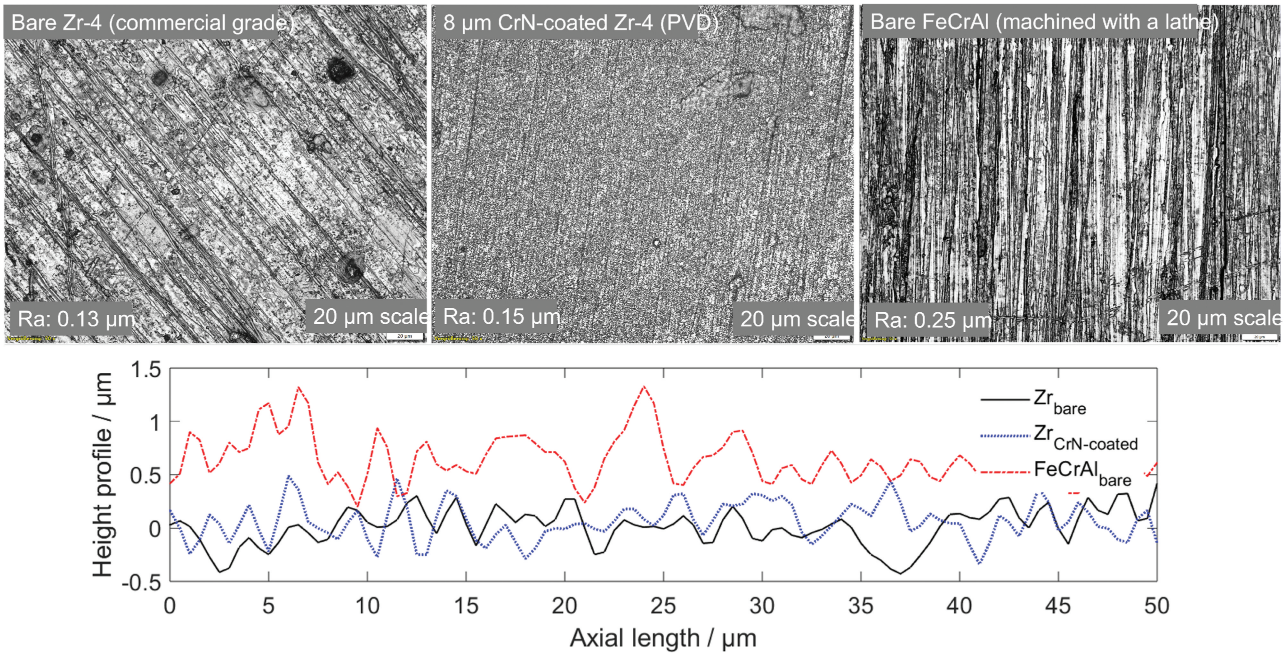

Fig. 3. Representative surface profile micrometers versus millimeters of the cladding tubes, measured by contact profilometry. A vertical offset was applied for clarity.

Based on a dual detection criterion comprising thermal and optical signals, CHF was identified. A CHF event was confirmed when a localized surface temperature increase of at least 20 K within 0.1 to 0.2 s was detected, together with visual evidence of vapor blanket formation or dry patch development captured by the high-speed camera, as shown in Fig. 4. Frame-by-frame video analysis was used to verify the stability and persistence of the dryout at the indicated location.

Following DNB onset, the affected surface region (typically 1 to 2 cm in diameter, depending on the response time of the detection threshold and transformer shutdown) experienced a rapid temperature overshoot of approximately 100 to 150 K before dropping back toward inlet temperature due to the loss of electrical heating. The 20 K trigger threshold thus represents a conservative yet robust detection limit: sufficiently sensitive to reliably capture the onset of boiling crisis while still low enough to prevent permanent surface damage and to allow repeated testing with the same rod bundle.

To ensure statistical robustness, a reference condition at $p = 1.2$ bars, $\Delta T_{\mathrm{sub}} = 25$ K, and $G = 400$ kg·m^{-2}·s^{-1} was measured 50 times using a Zr-4 cladding sample. The resulting CHF values were evaluated by fitting a Gaussian distribution, yielding a 3σ confidence interval of ±3.5%, which served as a benchmark for evaluating deviations at other test points. For all other operating conditions, each test point was repeated three times to estimate local variance and verify CHF onset within the experimental uncertainty.

Once a CHF event was detected, the associated video segment was reviewed to confirm persistent and localized dryout or overheating in the corresponding region. The synchronized data set, including temperature, heat flux, and optical recordings, enabled a clear correlation between thermal excursions and physical DNB. If the data and visual evidence were consistent, the corresponding heat flux value was designated as the CHF value for that test point. In cases where the transformer shutdown delay exceeded 0.3 s, irreversible surface marks (burn marks) were used to cross-validate the CHF location. The nondestructive nature of this method allowed for multiple CHF measurements on the same rod bundle, facilitating parametric studies without hardware replacement (see Fig. 5). The measurement matrix with the reference condition ($G = 200$ kg·m^{-2}·s^{-1}, $p = 1.4$ bar(a), $\Delta T_{\mathrm{sub}} = 18$ K) in the middle on which the present study is based is shown in Table II.

III.B. Measurement Uncertainty

Measurement uncertainties were evaluated using the classical error propagation methodology of Kline and McClintock.[25] This approach estimates the combined uncertainty of a derived quantity as a function of the uncertainties in the underlying measured parameters via a first-order Taylor series expansion. The relative uncertainty in a result $R = f(x_1, x_2, \ldots, x_n)$ is calculated as

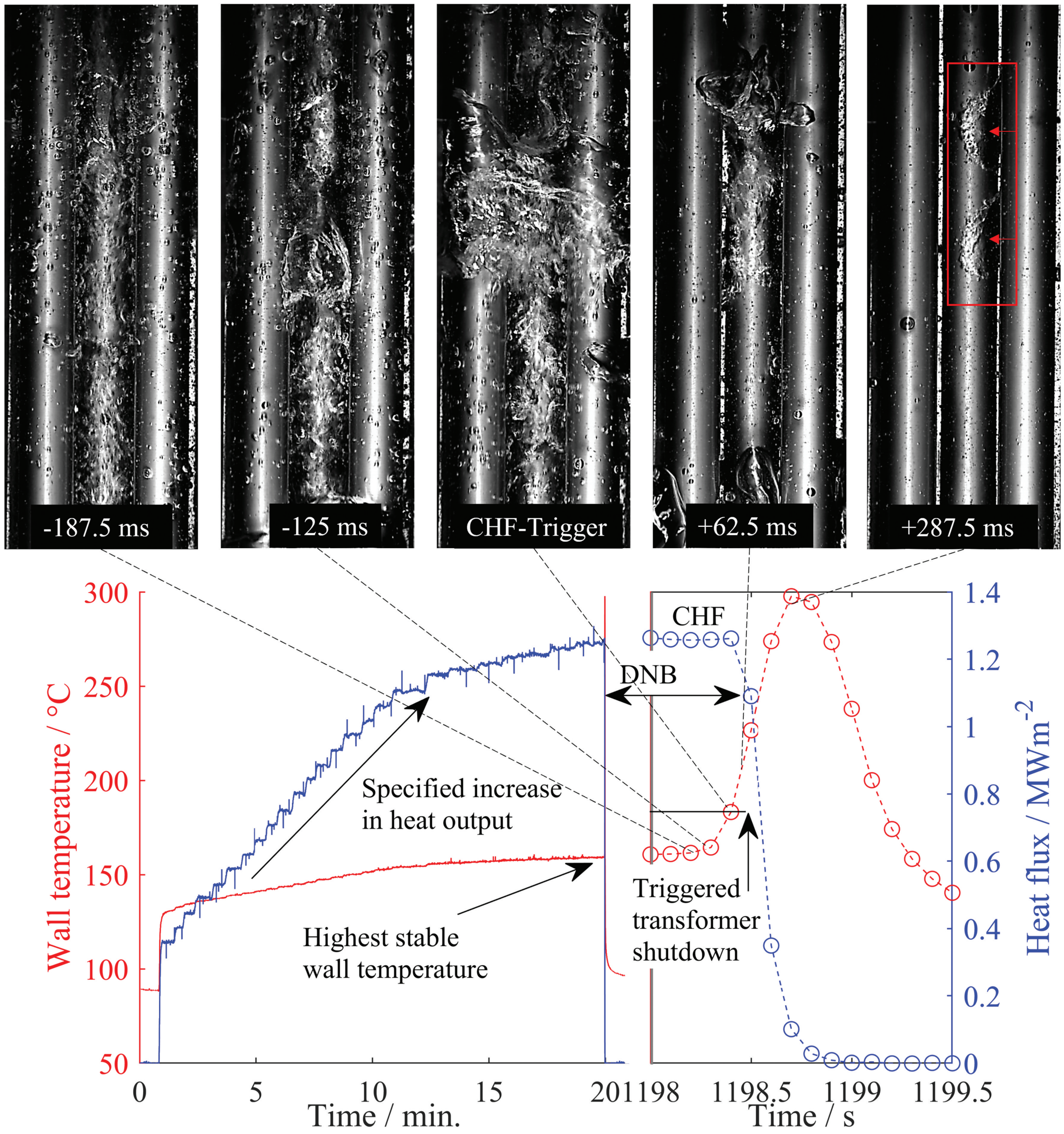

Fig. 4. Visual representation of the CHF measurement procedure, combining synchronized optical observation with temperature and heat flux logging at the CHF spot.

$$\frac{\Delta R}{R} = \sqrt{\left(\frac{\partial R}{\partial x_1}\cdot\frac{\Delta x_1}{R}\right)^2 + \left(\frac{\partial R}{\partial x_2}\cdot\frac{\Delta x_2}{R}\right)^2 + \ldots + \left(\frac{\partial R}{\partial x_n}\cdot\frac{\Delta x_n}{R}\right)^2}\,. \tag{1}$$

This expression accounts for both systematic and random error contributions. The main uncertainty sources and their representative values are as follows.

The mass flow rate was measured with a Coriolis flowmeter exhibiting a device-specified accuracy of ± 0.15%. Additional uncertainty arose from signal noise and manufacturing tolerances in test section geometry, particularly the tube diameter (9.5 ± 0.05 mm) and heated length (300 ± 0.1 mm). These resulted in a total uncertainty of $\pm 1.9\ \text{kg·m}^{-2}\text{·s}^{-1} + 0.38\%$ for the mass flux.

The pressure was monitored using a silicon-on-sapphire sensor [range: 0 to 2.5 bar(g)], with an overall precision of ± 0.4%, including linearity and hysteresis. Electrical interference from the heating system added noise, yielding a combined pressure uncertainty of approximately ± 45 mbars + 0.4%.

The temperature was measured with type K thermocouples (diameter: 0.34 mm), with uncertainty contributions from calibration (± 0.1 K), signal amplification

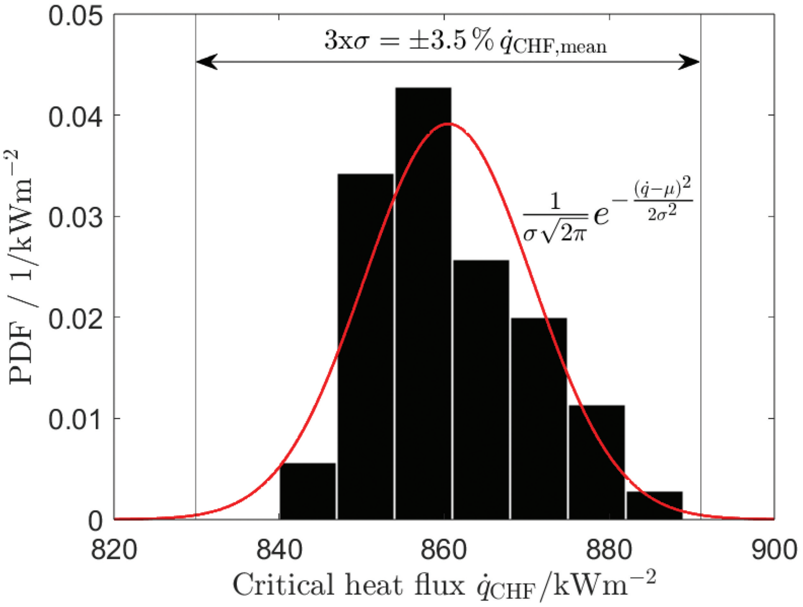

Fig. 5. Probability density function of the CHF values from 50 repeated measurements at the reference point. A normal distribution fit is shown in red.

(± 0.025% of reading + 0.4°C), and environmental noise (<0.5°C). The resulting uncertainty was ± 0.5 K $+ 0.15$ K across the operating range.

The heat flux was calculated from voltage and current measurements using a wattmeter (accuracy $\pm 0.3\%$) and a current transformer (accuracy $\pm 0.2\%$), along with geometric tolerances and AC waveform stability. The total relative uncertainty was evaluated as ± 0.01 MW·m^{-2} $+ 0.56\%$.

All uncertainties were propagated using the root-sum-square method and reported as expanded uncertainties with a coverage factor $k = 3$ (corresponding to a confidence level of 99.7%), unless otherwise stated. The 50-fold repetition of the reference point confirmed that the CHF variation is within $\pm 3.5\%$, underscoring the reproducibility and reliability of the measurement approach.

IV. MECHANISTIC CHF MODEL

IV.A. CHF Regime Classification and Model Framework

Under subcooled flow boiling conditions, Le Corre et al.[10] classify CHF into three distinct regimes: (1) bubbly flow–induced dryout at high subcooling and mass flux, (2) accumulation of vapor clot governed by interfacial instabilities under moderate conditions, and (3) intermittent dryout in slug flow near saturation. These regimes reflect different rewetting limitations and are

TABLE II

Test Matrix with Varied Boundary Conditions Around a Reference Point*

Case	Mass Flux, G (kg·m^{-2}·s^{-1})	Pressure, p [mbar(g)]	Subcooling, ΔT_{sub} (K)
Lower mass flux	100	400	18
Reference	200	400	18
Higher mass flux	400	400	18
Lower pressure	200	200	18
Higher pressure	200	800	18
Lower subcooling	200	400	9
Higher subcooling	200	400	36

*Each condition was tested for all cladding materials.

governed by parameters such as thermodynamic quality and the liquid Weber number. A comprehensive regime map and mechanistic interpretation are provided in their work and are consistent with previous visual studies by Jung and Kim[26] and instability-based CHF models such as Katto.

A plausible and established mechanistic modeling for the theorized type 3 CHF, which according to the Le Corres map, see Fig. 6, covers the entire experimental study of this thesis, is Katto's approach 2. This approach applied in this study assumes that the boiling crisis occurs when a thin microlayer of liquid, trapped beneath a growing vapor bubble, completely evaporates before rewetting can take place. The governing expression follows the formulation by Celata et al.[9] based on the original hypothesis by Katto. The CHF is expressed as

$$\dot{q}_{\mathrm{CHF}} = \frac{\rho_\ell \cdot \delta \cdot \Delta h_{\mathrm{lv}}}{\tau_B} = \frac{\rho_\ell \cdot \delta \cdot \Delta h_{\mathrm{lv}} \cdot U_B}{L_B}, \qquad (2)$$

where ρ_ℓ = density of the liquid phase; δ = microlayer thickness beneath the vapor bubble; Δh_{lv} = latent heat of vaporization; τ_B = bubble growth or residence time; U_B = vapor blanket or bubble departure velocity; L_B = characteristic length of the vapor blanket, which can be associated with the instability wavelength of the vapor-liquid interface.

In this context, L_B is approximated by the critical wavelength of the Kelvin-Helmholtz instability:

$$L_B = \lambda_{\mathrm{KH,crit}} = 2\pi\sqrt{\frac{\sigma}{g(\rho_\ell - \rho_v)}}, \qquad (3)$$

where σ = surface tension; g = gravitational acceleration; ρ_v = vapor density. This relation reflects the most unstable mode of interfacial perturbation between two phases with different densities. The bubble velocity U_B can be estimated from force balances used by Celata et al.[9] and in the present work or empirical correlations, often as a function of Jakob number and wall superheat.

The boundary conditions for which the model is considered valid include thermodynamic quality in the range of $-0.3 < X_{\mathrm{th}} < 0.05$, a liquid Weber number between 10^2 and 10^4, and stable bubbly to churn flow regimes.

If the type 3 CHF regime in Fig. 6 is exceeded, as is the case for the test condition "2x reference subcooling" in this study, the prediction quality for all three cladding tube cases falls in comparison to the other test conditions, which can be seen in the range −45 to −35 kW in Fig. 7.

IV.B. Empirical Scaling of Microlayer Thickness

The original implementation of Celata et al.'s model involved estimating the sublayer thickness δ via a temperature profile derived from Martinelli's internal tube flow theory.[9] However, in the low-pressure and highly subcooled conditions examined here, this approach yielded nonphysical or diverging microlayer

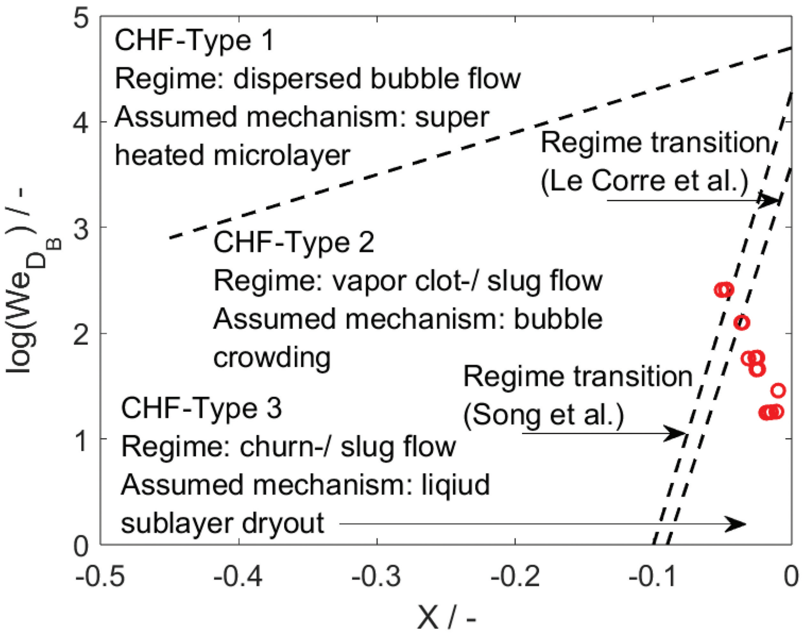

Fig. 6. CHF regime map after Le Corre et al.[10] with red markers indicating experimental conditions. All data points lie within the liquid sublayer dryout domain.

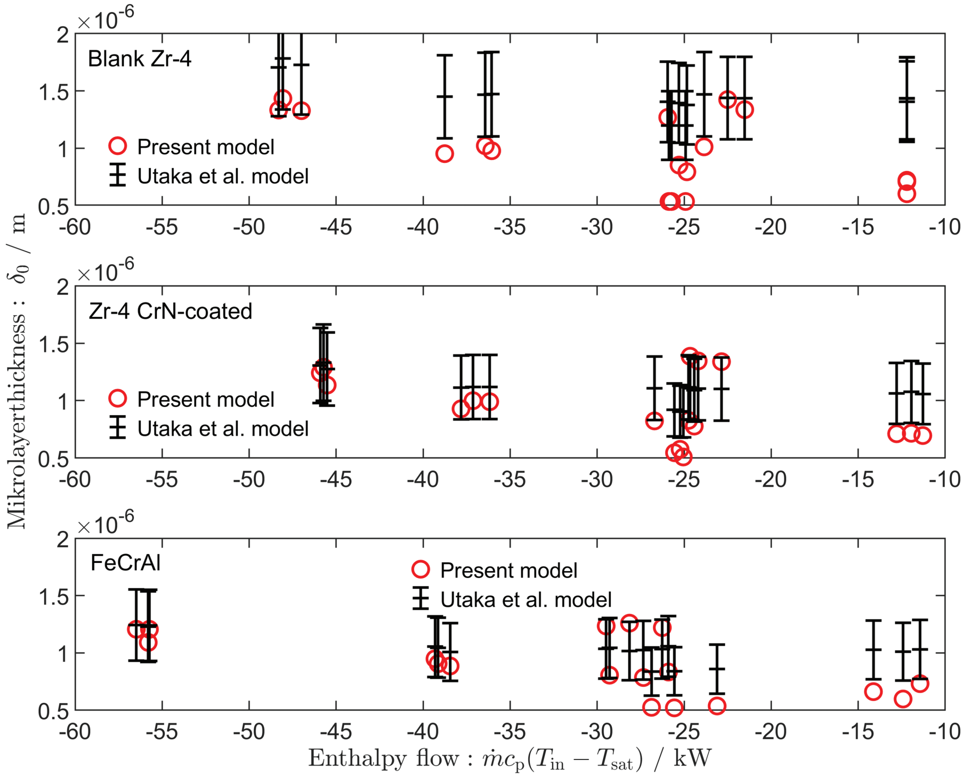

Fig. 7. Comparison of calculated microlayer thickness δ using the present scaling (red) and the correlation by Utaka et al. [28] (black) across all test points. The present model avoids divergence at low mass flux and aligns better with measured CHF trends.

values and showed poor numerical convergence, particularly at low mass fluxes.

To overcome these issues, a new empirical scaling relation for the maximum microlayer δ in the liquid converging gap below a growing vapor bubble in the sense of, e.g., Refs. [27] and [28], replacing the liquid sublayer between the heated wall and a passing vapor blanket, was developed. Here, the breakup time of a bubble replaces the hovering time of the vapor blanket above an imminent drying-out location (DNB). This revised model incorporates material-specific surface parameters, such as contact angle β_{wet} and critical cavity diameter D_c, as well as fluid properties and system conditions. The proposed scaling law reads as

$$\delta = C \cdot \pi \cdot D_c \cdot (1 - \cos\beta_{\mathrm{wet}}) \cdot \left(\frac{X_{\mathrm{th}}}{X_{\mathrm{ref}}} \cdot \sqrt{\frac{c_{p,w}}{c_{p,w,\mathrm{ref}}}} \right)^{1/\mathrm{Pr}} , \tag{4}$$

where β_{wet} = static contact angle that characterizes wettability of the surface; D_c = critical cavity diameter for stable nucleation; X_{th} = thermodynamic quality normalized by the mass flux; Pr = Prandtl number of the liquid phase. The specific heat of the wall material $\sqrt{c_{p,w}}$ enters as a correction factor accounting for transient thermal penetration in case of a DNB and is inspired from the thermal effusivity $\sqrt{\rho_w \cdot \lambda_w \cdot c_{p,w}}$. The constant C is determined from calibration at a known reference condition (Zr-4 at 1.4 bar, 18 K subcooling, and $200\ \mathrm{kg \cdot m^{-2} \cdot s^{-1}}$) and remains fixed for all other evaluations in the present work to $C = 0.3$.

The critical cavity diameter D_c is derived from capillarity and buoyancy balance and is given by

$$D_c = \frac{4 \cdot \sigma \cdot \cos\beta_{\mathrm{wet}}}{\rho_l \cdot g \cdot (T_{\mathrm{sat}} - T_w)} , \tag{5}$$

where T_{sat} is the saturation temperature at the local pressure and T_w is the wall surface temperature. This expression reflects the maximum diameter of a cavity that can support stable vapor embryo growth under the influence of capillary and hydrostatic forces.

Physically, the term $\pi D_c (1 - \cos\beta_{\mathrm{wet}})$ in Eq. (4) represents the wettability modulated anchoring force between the wall and the base of the vapor bubble. The quality ratio $X_{\mathrm{ref}}/X_{\mathrm{th}}$ scales the thermal driving potential relative to the calibrated case. The use of the Prandtl number in both thermodynamic and heat capacity scaling ensures that diffusion-dominated transient behavior is taken into account across different material properties.

The calculated microlayer thicknesses were compared with those obtained from the model by Utaka et al.[28] commonly used in microscale boiling analyses. As shown in Fig. 8, the present model avoids divergences at low subcooling and provides physically consistent results within the uncertainty of ±25% specified by Utaka et al.[28] for the parameter space investigated.

The developed model is applicable to subcooled or low-quality boiling regimes in vertical upward flow through rod bundles, particularly for conditions where $100 < \mathrm{We}_\ell < 10^4$ and $-0.3 < X_{\mathrm{th}} < 0.05$. It is not suitable for strongly asymmetric heating, annular dryout regimes, or dynamic rewetting phenomena.

V. RESULTS

V.A. CHF Sensitivity and Unified Scaling with Enthalpy Flux

To assess the influence of individual thermal-hydraulic parameters on CHF, all three investigated cladding materials, i.e., Zr-4, CrN-coated Zr-4, and FeCrAl, were tested across a matrix of seven operating conditions. These include halved and doubled values of pressure, mass flux, and inlet subcooling around a defined reference point ($p = 1.4$ bar, $\Delta T_{\mathrm{sub}} = 18$ K, $G = 200\ \mathrm{kg{\cdot}m^{-2}{\cdot}s^{-1}}$), as specified in the test matrix Table II. Each condition was repeated three times; the reference was measured 50 times to quantify statistical confidence.

While this parametric variation demonstrates the expected monotonic CHF response to mass flux and subcooling, its combinatorial nature limits generalizability. To reduce complexity and enable a unified interpretation of the data, the enthalpy flux differential $\dot{H} = G \cdot c_p \cdot (T_{\mathrm{in}} - T_{\mathrm{sat}})$ was introduced. This parameter consolidates the thermal driving potential for boiling onset into a single expression and implicitly includes pressure, subcooling, and mass flux effects via the thermodynamic state of the fluid.

The CHF values plotted against $\dot{H}$ reveal a predominantly linear trend across the investigated range for all three cladding types. Figure 9 shows that both Zr-4 and CrN-coated Zr-4 exhibit nearly parallel linear regressions, suggesting a consistent sensitivity of CHF to enthalpy flux variation. The FeCrAl samples, however, display a slightly altered slope, indicating a deviation from the otherwise uniform scaling behavior. Regression details are provided in Table III.

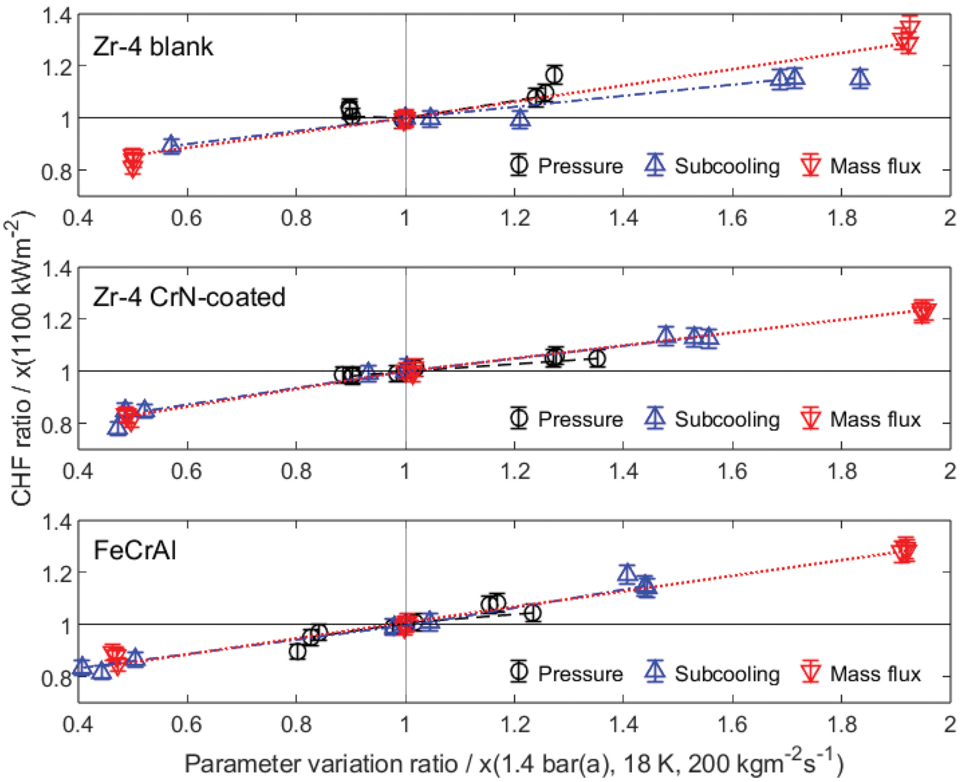

Fig. 8. CHF response for all cladding materials under parameter variation. The nearly parallel slopes suggest uniform sensitivity to external thermal-hydraulic conditions.

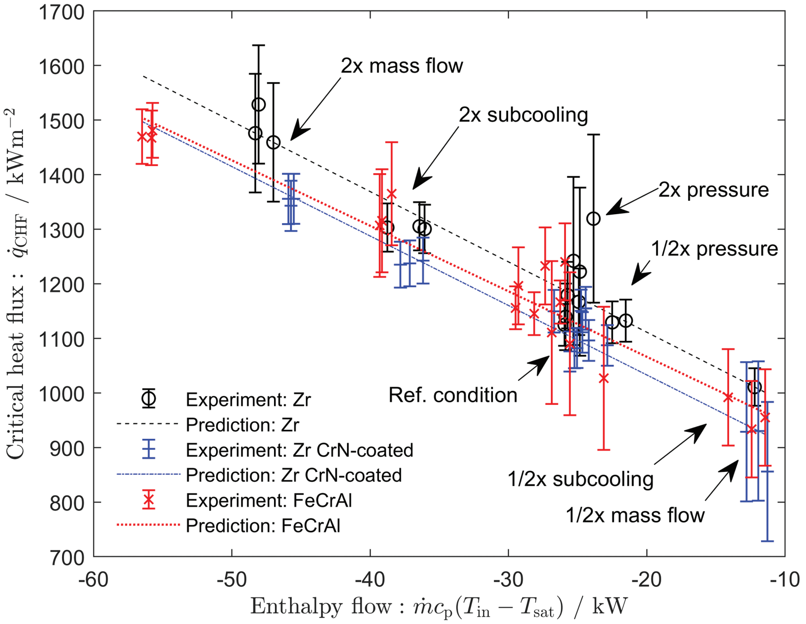

Fig. 9. CHF plotted against enthalpy flux $\dot{H}$ for each cladding material. Linear regressions illustrate differences in absolute CHF offset and slope.

This deviation becomes more evident when analyzing the predicted microlayer thickness δ as a function of enthalpy flux, as shown in Fig. 10. The FeCrAl data reveal a material-specific trend in δ, deviating from the linear scaling observed for the other two claddings. While the proposed model accurately captures the measured CHF for all three materials, this non-parallel behavior in CHF–$\dot{H}$ space reflects differences in the surface-driven response embedded in the mechanistic formulation.

This trend of decreasing microlayer thickness with increasing $\dot{H}$ for FeCrAl compared to the Zr-4–based rod bundles is consistent with the empirically observed CHF behavior: The onset of dryout occurs earlier for thinner microlayers, which is reflected in the progressive tilting of the CHF response curve for FeCrAl in Fig. 11 and in the normalized sensitivities summarized in Table IV. These results suggest that while Zr-4 and the present 8-µm CrN-coated Zr-4 maintain a material-invariant microlayer stability against the DNB over the investigated range, FeCrAl exhibits a more condition-dependent response. In the present scaling approach, the observed reduction in microlayer thickness at elevated enthalpy flux deficits—and the associated tilt in CHF sensitivity—can be traced back primarily to the intrinsically lower wetting angle of the FeCrAl surface. This initial wettability disadvantage cannot be compensated by temperature-based corrections or the inclusion of heat capacity in the model in comparison to the other tested rod bundle variants. As a result, the stability of the microlayer diminishes under increasing $\dot{H}$, leading to an earlier DNB. These findings highlight that surface wettability acts as a key limiting factor in CHF scaling for bulk ATF materials, particularly when diverging from the thermal and topological characteristics of Zr-based reference claddings.

V.B. Prediction Model Evaluation

To evaluate the material-sensitive CHF prediction model described in Sec. IV, a quantitative comparison

TABLE III

Linear Regression Equations for CHF as a Function of Enthalpy Flux $\dot{H}$, with Regression Quality Metrics

Cladding Material	Regression Equation, $\dot{q}_{\mathrm{CHF}}$ (kW·m^{-2})	r^2	Root-Mean-Square Error
Zr-4	$-12.886 \cdot \dot{H} + 853.55$	0.981	22.2
CrN-coated Zr-4	$-12.730 \cdot \dot{H} + 778.32$	0.950	32.0
FeCrAl	$-12.004 \cdot \dot{H} + 826.10$	0.925	48.9

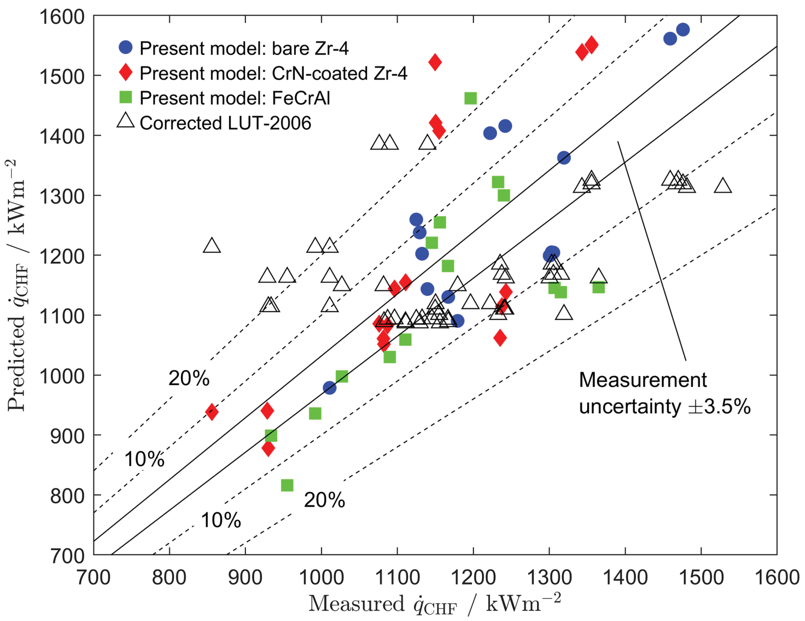

Fig. 10. Comparison of predicted versus measured CHF for all materials using the mechanistic microlayer model, with the measured CHF uncertainty of ±3.5%.

between the predicted and the measured CHF values was conducted. Figure 7 shows the predicted CHF versus experimental results for all material cases using the mechanistic microlayer dryout model. The model accounted for relevant surface properties, including contact angle (corrected temperature per Li[29] and Adamson[30]), roughness, thermal diffusivity, and cavity distribution.

In addition to the mechanistic model evaluation, the LUT-2006 of Groeneveld[7] was employed as a widely accepted empirical benchmark to assess the baseline CHF prediction capability. Since the LUT is inherently formulated for uniformly heated vertical tubes, its application to the present rod bundle configuration required correction. To account for the geometric and hydraulic differences,

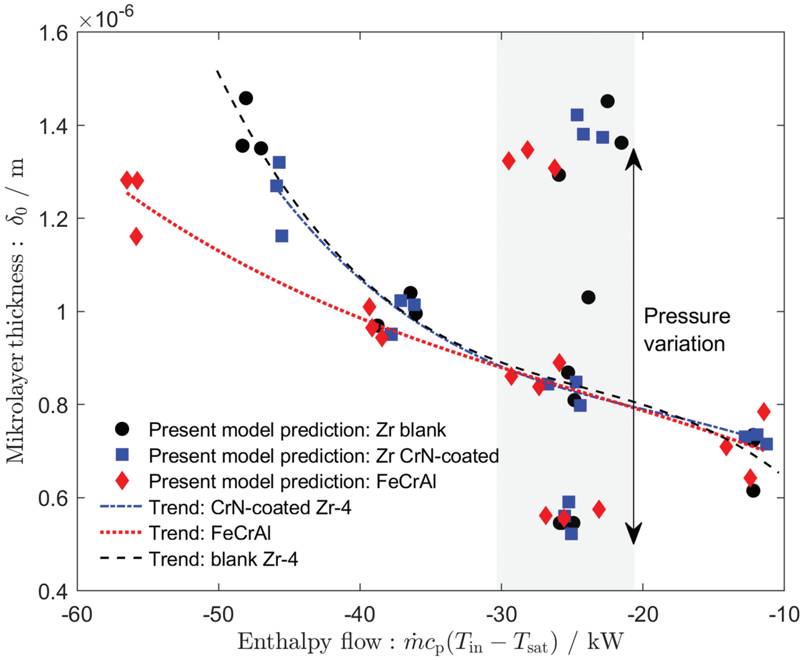

Fig. 11. Predicted microlayer thickness δ as a function of enthalpy flux $\dot{H}$ for all cladding materials. While Zr-4 and CrN-coated Zr-4 show nearly identical trends, FeCrAl exhibits a decreasing δ with increasing $\dot{H}$, indicating reduced microlayer stability against the DNB at high thermal loads.

TABLE IV

Normalized CHF Sensitivity Across Materials

Material	CHF Ratio (Doubled/ Halved)
Bare Zr-4	0.68
CrN-coated Zr-4	0.63
FeCrAl	0.67

standard K-factors were applied, as specified in the International Atomic Energy Agency report[31] enabling the extrapolation of tube-based CHF predictions to rod bundle conditions. These bundle correction factors, denoted as K_{bundle}, are defined as the ratio between CHF in rod bundle geometry and CHF in equivalent tube geometry under identical thermal-hydraulic conditions, i.e., $\dot{q}_{\text{CHF,bundle}} = K_{\text{bundle}} \cdot \dot{q}_{\text{CHF,tube}}$. The values of K_{bundle} are tabulated in the LUT documentation as a function of pressure, mass flux, and bundle geometry. They account for effects such as subchannel interactions and nonuniform flow distribution and are commonly used in reactor safety analysis to provide conservative CHF estimates for fuel assembly evaluations.

Overall, the model demonstrated strong agreement with the experimental data. The mean absolute percentage errors (MAPEs) were 6.8% for Zr-4, 10.2% for CrN-coated Zr-4, and 8.8% for FeCrAl. The predictions remained within the ± 25% tolerance band proposed by Utaka et al.[28] confirming the applicability of the model. For comparison, the LUT-2006 achieves 10.3% (Zr-4), 8.9% (CrN-coated Zr-4), and 12% (FeCrAl) for generally surface-unspecific conditions and thus has slightly lower measured value agreements. Complementary to this mechanistic interpretation, the Groeneveld LUT was used as a reference benchmark. While the LUT provided CHF estimates within acceptable ranges and served as a consistent orientation baseline, its inherent material insensitivity became evident. Specifically, it failed to capture the moderate but systematic CHF differences induced by surface modifications such as the CrN coating. In contrast, the developed model retained predictive accuracy (MAPE $< 10\%$) while preserving physical interpretability and parameter separation.

It is assumed that because of its large empirical basis (>25 000 CHF data points across 62 datasets collected over 60 years[7]), the LUT statistically averages out material- and surface-specific deviations within its interpolation domain. Furthermore, it was primarily designed to cover high CHF levels, typically associated with pressurized water reactor near pressures, mass fluxes, and enthalpy fluxes $\dot{H}$. In such regimes, the relative impact of surface microstructure tends to diminish. In contrast, the present experimental and modeling framework targets low-pressure, subcooled boiling conditions, where surface effects remain pronounced. While the proposed mechanistic model offers greater sensitivity to these influences, it exhibits a slight overprediction tendency, particularly for the CrN-coated cladding tubes. This suggests that although well suited for capturing material trends, further refinement may be needed to improve quantitative CHF estimates for coated surfaces under marginal boiling conditions.

VI. DISCUSSION

VI.A. Material Influence and Model Interpretation

While no direct one-to-one correlation was found between CHF and individual descriptors such as R_a, R_z, or mean contact angle, the integration of these surface characteristics into the mechanistic model revealed indirect scaling effects. In particular, the heat capacity c_p entered the microlayer scaling of the model through $\sqrt{c_p}$, representing the transient thermal response. This formulation improved predictive performance and aligns with the experimentally observed CHF differentiation among materials.

The low thermal conductivity of the CrN coating ($2.0\ \text{W}\cdot\text{m}^{-1}\cdot\text{K}^{-1}$), despite its limited thickness, may locally influence the heat flux distribution and nucleation dynamics. Although no explicit conductivity-based correction was included in the model, the reduced CHF offset for CrN-coated Zr-4 is qualitatively consistent with such effects. It is assumed that in the present case of an 8-μm-thin CrN layer, the diminished ability to laterally redistribute local heat fluxes, especially in the presence of incipient dryout or vapor patches, plays a subordinate but non-negligible role. Thin surface coatings with low thermal conductivity, such as CrN, are inherently limited in their ability to spread heat laterally at the microscale. This becomes particularly relevant near the boiling crisis, where localized hotspots may emerge rapidly and trigger premature dryout. Theoretical and experimental studies have highlighted this limitation in the context of bubble dynamics and nanoscale thermal transport by Kim[32] and Cahill et al.[33] The coating's limited thickness likely reduces its capacity to buffer such transients, contributing to the slight downward shift in CHF observed for CrN-coated samples.

When analyzing the CHF response as a function of enthalpy flux $\dot{H}$, Zr-4 and CrN-coated Zr-4 exhibit nearly parallel linear trends, indicating a comparable sensitivity of CHF to the thermal driving potential across these two materials. FeCrAl, by contrast, shows a progressively deviating behavior with increasing $\dot{H}$, manifesting in a flatter slope. This trend is reflected in the microlayer thickness predictions of the mechanistic model (Fig. 10), which consistently yield thinner δ values for FeCrAl and CrN-coated Zr-4 than for uncoated Zr-4 under equivalent conditions. These thinner microlayers suggest a reduced liquid reservoir beneath the growing vapor bubbles and thus a higher likelihood of earlier dryout onset, consistent with the observed CHF levels of Fig. 11.

A closer comparison shows that CrN-coated Zr-4 maintains a nearly constant CHF offset relative to bare Zr-4 across the entire tested $\dot{H}$ range. FeCrAl, however, initially aligns with the CHF behavior of the Zr-based samples but gradually diverges with increasing enthalpy flux deficit toward saturation. This material-dependent shift is accurately captured by the model, confirming that the experimentally observed CHF response governs, and is mirrored in, the microlayer dynamics predicted for each cladding variant.

Within the current model framework, this effect is plausibly explained by the role of wettability and roughness in modifying bubble dynamics and rewetting behavior. The use of the thermodynamic quality X_{th}, derived from the enthalpy difference to saturation and normalized by mass flux, further enables the model to absorb these nonlinearities in a physically meaningful way. Thus, even though FeCrAl does not follow the same linear CHF–$\dot{H}$ sensitivity as the coated and uncoated Zr-4, the model is capable of reproducing its behavior within acceptable error margins.

Complementary to this mechanistic interpretation, the Groeneveld LUT was used as a reference benchmark. While the LUT provided CHF estimates within acceptable ranges and served as a consistent orientation baseline, its inherent material insensitivity became evident. Specifically, it failed to capture the moderate but systematic CHF differences induced by surface modifications such as the CrN coating. In contrast, the developed model retained predictive accuracy (MAPE <10%) while preserving physical interpretability and parameter separation. This underscores the advantage of physics-informed approaches in evaluating ATF claddings, where subtle yet consequential differences in surface energy, wettability, and heat transfer response govern boiling crisis onset.

VI.B. Validation Framework and Data Utility

The structured test matrix, statistical rigor, and optical verification implemented in this work produced a coherent and reproducible dataset. This quality is critical for validating mechanistic models and addressing previously reported deviations between laboratories up to 30%.[7] The agreement between measured and predicted CHF values using the Celata et al.–based framework demonstrates how surface-modified ATF claddings can be systematically assessed in model development.

Within its applicable range, the model reproduced material trends and absolute CHF values with prediction errors typically below 10%, which is comparable to or better than generalized tools such as the Groeneveld LUT.[7] However, in contrast to such generalized approaches, the present model accounts explicitly for surface-specific parameters and material properties, making it suitable for evaluating advanced cladding concepts such as ATF materials.

VII. CONCLUSION

This work contributes to the ongoing effort of characterizing CHF behavior for ATF cladding materials by providing a statistically validated and reproducible dataset based on systematic comparisons between coated and bulk ATF concepts. While previous studies have addressed CHF in simplified configurations, the present investigation offers complementary evidence by focusing on five-rod bundle experiments under controlled subcooled flow boiling conditions representative of simplified LWR environments. Unlike annular gap or internally heated tube geometries, this setup enables direct material comparison in a bundle-relevant but still well-controlled thermohydraulic context.

The findings show that surface-engineered coatings and bulk alloy substitutions influence CHF performance in distinct ways. Statistically significant differences of up to 8.8% were observed for CrN-coated Zr-4 compared to its uncoated counterpart, while FeCrAl showed a nonsignificant deviation of 3.2%. These moderate but consistent trends suggest that local surface characteristics, particularly wettability and thermal effusivity, play a more decisive role in initiating boiling crisis than do bulk thermal properties alone.

To interpret these results, a mechanistic CHF model based on microlayer dryout theory was developed and tailored to material-specific parameters. The model reproduced the measured CHF values with MAPEs of 6.7% (Zr-4), 10.2% (CrN-coated Zr-4), and 8.8% (FeCrAl), within the accuracy range of ± 25% proposed in the literature for the primarily new microlayer subrelationship in the proposed mechanistic CHF model. This confirms the model's capacity to capture material-induced CHF trends similar or beyond empirical correlations such as the widly used Groeneveld LUT with 10.3% (Zr-4), 8.9% (CrN-coated Zr-4), and 12% (FeCrAl), which neglect surface effects.

Taken together, these results reinforce the importance of surface thermophysical properties in ATF evaluation and demonstrate that predictive mechanistic modeling can be extended to novel cladding concepts with appropriate calibration.

Building on this foundation, future work may extend the current investigations toward the post-CHF regime to assess material-specific differences in dryout propagation and surface recovery behavior. Complementary characterization techniques such as scanning electron microscopy applied to dried-out regions could offer further insights into irreversible surface alterations and defect evolution at the microscale. Additionally, direct quantification of key boiling-related surface parameters, including nucleation site density, bubble departure frequency, and departure diameter, would support a more detailed mechanistic understanding of surface-governed CHF processes. Expanding the current framework to cover pressure and thermal-hydraulic regimes relevant to pressurized and boiling water reactors would further enhance its relevance for ATF qualification and safety evaluation.

Acronyms

AC: alternating-current
ATF: accident-tolerant fuel
CHF: critical heat flux
COSMOS-L: Critical heat flux On Smooth and MOdified Surfaces – Low pressure
CrN: chromium nitride
DNB: departure from nucleate boiling
FeCrAl: iron chromium aluminum (alloy)
LUT: look-up table
LWR: light water reactor
MAPE: mean absolute percentage error
Zr-4: Zircaloy-4

Nomenclature

A = cross-sectional area (m^2)
C = calibration factor in microlayer model
D_c = critical cavity diameter (m)
h_{in} = inlet enthalpy ($\mathrm{J \cdot kg^{-1}}$)
h_{sat} = saturation enthalpy ($\mathrm{J \cdot kg^{-1}}$)
L = heated length or slab thickness (m)
L_B = vapor blanket length (m)
= mass flux ($\mathrm{kg \cdot m^{-2} \cdot s^{-1}}$)
Pr = Prandtl number
p = pressure (bar)
$\dot{q}_{\mathrm{CHF}}$ = critical heat flux ($\mathrm{kW \cdot m^{-2}}$)
R = general derived variable
R_a = arithmetic mean roughness (μm)
R_z = peak-to-valley roughness (μm)
r^2= coefficient of determination
T = temperature (K or °C)
U_{B} = vapor blanket velocity ($\mathrm{m \cdot s^{-1}}$)
We = Weber number
X_{ref} = reference thermodynamic quality
X_{th} = thermodynamic quality
$[.]B$ = bubble-related quantity
$[.]l$, $[.]v$ = liquid or vapor property
$[.]ref$ = reference condition
$[.]w$ = wall-related quantity

Greek

β_{wet} = static contact angle (deg)
Δh_{lv} = latent heat of vaporization ($\mathrm{J \cdot kg^{-1}}$)
ΔT_{sub} = subcooling (inlet, saturation) (K)
Δx = measurement uncertainty
δ = microlayer thickness (m)
λ = thermal conductivity ($\mathrm{W \cdot m^{-1} \cdot K^{-1}}$)
$\lambda_{\mathrm{KH,crit}}$ = Kelvin-Helmholtz critical wavelength (m)
ρ = density ($\mathrm{kg \cdot m^{-3}}$)
σ = surface tension or statistical deviation
τ_{B} = bubble residence time (s)

Acknowledgments

The authors thank the German Society for Plant and Reactor Safety and the German Federal Ministry for Economic Affairs and Energy as part of the KEK program, which financially supports this work. The authors also thank the members of the Multiphase Flows Department and Framatome Professional School (for their support in technical matters. This work was also supported by the OFFERR COATED. Furthermore, the authors confirm that some aspects of text editing were supported by an AI language model (GPT-4) to improve readability.

Author Contributions

CRediT: **Nicolas Wefers:** Formal analysis, Investigation, Methodology, Visualization, Writing – original draft, Writing – review & editing; **Daniel Vlček:** Conceptualization, Validation, Writing – review & editing; **Wilson Heiler:** Investigation, Validation, Writing – review & editing; **Stephan Gabriel:** Conceptualization, Data curation, Funding acquisition, Resources, Supervision; **Andreas Class:** Conceptualization, Methodology, Supervision.

Data Availability Statement

Data will be made available on request.

Funding

This work was supported by the GRS under grant 1501646.

Declaration of Competing Interests

The authors declare the following financial interests/personal relationships that may be considered as potential competing interests. Nicolas Wefers reports financial support was provided by the GRS. If there are other authors, they declare that they have no known competing financial interests or personal relationships that could have appeared to influence the work reported in this paper.

ORCID

Nicolas Wefers http://orcid.org/0009-0003-9116-2063
Daniel Vlček http://orcid.org/0000-0002-7267-1511

References

1. L. S. TONG and J. WEISMAN, *Thermal Analysis of Pressurized Water Reactors*, American Nuclear Society (1997).
2. J.-C. BRACHET et al. “Behavior Under LOCA Conditions of Enhanced Accident Tolerant Chromium Coated Zircaloy-4 Claddings,” *Proc. Light Water Reactor Fuel Performance Mtg. (Topfuel 2016)*, Boise, Idaho, September 11–15, 2016, American Nuclear Society (2016).
3. F. GOLDNER et al., “The U.S. Accident Tolerant Fuels Program—Update on a National Initiative,” U.S. Department of Energy (2022).
4. M. ŠEVEČEK et al., “Development of Cr Cold Spray–Coated Fuel Cladding with Enhanced Accident Tolerance,” *Nucl. Eng. Technol.*, **50**, *2*, 229 (2018); https://doi.org/10.1016/j.net.2017.12.011.
5. L. A. KARPYUK et al., “Accident Tolerant Fuel with Chromium-Coated Fuel-Rod Cladding,” *Atomic Energy*, **130**, *3*, 149 (2021); https://doi.org/10.1007/s10512-021-00786-9.
6. C. KIM et al., “Oxidation Mechanism and Kinetics of Nuclear-Grade FeCrAl Alloys in the Temperature Range of 500–1500°C in Steam,” *J. Nucl. Mater.*, **564**, 153696 (2022); https://doi.org/10.1016/j.jnucmat.2022.153696.
7. D. C. GROENEVELD et al., “The 2006 CHF Look-Up Table,” *Nucl. Eng. Des.*, **237**, *15–17*, 1909 (2007); https://doi.org/10.1016/j.nucengdes.2007.02.014.
8. Y. KATTO, “A Physical Approach to Critical Heat Flux of Subcooled Flow Boiling in Round Tubes,” *Int. J. Heat Mass Transfer*, **33**, *4*, 611 (1990); https://doi.org/10.1016/0017-9310(90)90160-V.
9. G. CELATA et al., “Rationalization of Existing Mechanistic Models for the Prediction of Water Subcooled Flow Boiling Critical Heat Flux,” *Int. J. Heat Mass Transfer*, **37**, 347 (1994); https://doi.org/10.1016/0017-9310(94)90035-3.
10. J.-M. LE CORRE, S.-C. YAO, and C. H. AMON, “Two-Phase Flow Regimes and Mechanisms of Critical Heat Flux Under Subcooled Flow Boiling Conditions,” *Nucl. Eng. Des.*, **240**, *2*, 245 (2010); https://doi.org/10.1016/j.nucengdes.2008.12.008.
11. M. DUAN et al., “An Experimental Research of the Influence on Critical Heat Flux of a Rod Bundle Under Certain Inlet Temperatures,” *Front. Energy Res.*, **12**, 1340675 (2024); https://doi.org/10.3389/fenrg.2024.1340675.
12. A. K. RAO and H. POTHUKUCHI, “Critical Heat Flux in a Rod Bundle Operating at Low Pressure Conditions,” *Int. J. Numer. Methods Heat Fluid Flow*, **35**, *5*, 1713 (2025); https://doi.org/10.1108/HFF-01-2025-0032.
13. S. CHEN et al., “An Experimental Study on Critical Heat Flux for Low Flow and Low Pressure of Water in a Hexagonal 7-Rod Bundle Channel,” *Prog. Nucl. Energy*, **171**, 105154 (2024); https://doi.org/10.1016/j.pnucene.2024.105154.
14. A. ALI et al., “Ion Irradiation Effects on Cr-Coated Zircaloy-4 Surface Wettability and Pool Boiling Critical Heat Flux,” *Nucl. Eng. Des.*, **362**, 110581 (2020); https://doi.org/10.1016/j.nucengdes.2020.110581.

15. K. BARRETT, S. BRAGG-SITTON, and D. GALICKI, “Advanced LWR Nuclear Fuel Cladding System Development Trade-Off Study,” INL/EXT-12-27090, Idaho National Laboratory (2012).
16. G. SU, M. BUCCI, and P. SABHARWALL, “Investigations on the Thermal-Hydraulic Behavior of Accident Tolerant Fuel Cladding Materials,” Idaho National Laboratory (2020); https://doi.org/10.2172/1594995.
17. D. LEE et al., “Enhanced Flow Boiling Heat Transfer on Chromium Coated Zircaloy-4 Using Cold Spray Technique for Accident Tolerant Fuel (ATF) Materials,” *Appl. Therm. Eng.*, **185**, 116347 (2021); https://doi.org/10.1016/j.applthermaleng.2020.116347.
18. C. CHEN et al., “Study on Heat Transfer and Bubble Behavior Inside Horizontal Annuli: Experimental Comparison of R-134a, R-407C, and R-410A Subcooled Flow Boiling,” *Case Studies Therm. Eng.*, **24**, 100875 (2021); https://doi.org/10.1016/j.csite.2021.100875.
19. C. CHEN et al., “Experimental Study on R-410A Subcooled Flow Boiling Heat Transfer and Bubble Behavior Inside Horizontal Annuli,” *Int. Commun. Heat Mass Transfer*, **124**, 105283 (2021); https://doi.org/10.1016/j.icheatmasstransfer.2021.105283.
20. F. KAISER, Y. SATO, and S. GABRIEL, “Subcooled Forced Convection Boiling Flow Measured Using High-Resolution Techniques at the COSMOS-L Facility and Accompanying CFD Simulation Employing an Interface-Tracking Scheme,” *Int. J. Multiph. Flow*, **174**, 104772 (2024); https://doi.org/10.1016/j.ijmultiphaseflow.2024.104772.
21. “Thermal Conductivity and Electrical Resistivity of Zircaloy-4 Tubes and Plates,” Pub176826, Oak Ridge National Laboratory (2016).
22. J. CHASE, *NIST-JANAF Thermochemical Tables*, 4th ed., American Institute of Physics (1998).
23. Kanthal APM – Resistance Heating Wire and Resistance Wire, Kanthal website (2024); https://www.kanthal.com/en/products/datasheets/material-datasheets/wire/resistance-heating-wire-and-resistance-wire/kanthal-apm/ (accessed May 9, 2024).
24. MATPRO—A Library of Materials Properties for Light-Water-Reactor Accident Analysis NUREG/CR-6150, Rev 2, Vol. 4, U.S. Nuclear Regulatory Commission (2001).
25. S. J. KLINE and F. A. MCCLINTOCK, “Describing Uncertainties in Single-Sample Experiments,” *Mech. Eng.*, **75**, *1*, 3 (1953).
26. S. JUNG and H. KIM, “Observation of the Mechanism Triggering Critical Heat Flux in Pool Boiling of Saturated Water Under Atmospheric Pressure,” *Int. J. Heat Mass Transfer*, **128**, 229 (2019); https://doi.org/10.1016/j.ijheatmasstransfer.2018.08.128.
27. Z.-X. SHEN et al., “Experimental Investigation of the Microlayer and Dry Spot Dynamic Characteristics in a Small Channel Flow Boiling by Laser Interferometry Method,” *Int. J. Heat Mass Transfer*, **201**, 123585 (2023); https://doi.org/10.1016/j.ijheatmasstransfer.2022.123585.
28. Y. UTAKA, Y. KASHIWABARA, and M. OZAKI, “Microlayer Structure in Nucleate Boiling of Water and Ethanol at Atmospheric Pressure,” *Int. J. Heat Mass Transfer*, **57**, *1*, 222 (2013); https://doi.org/10.1016/j.ijheatmasstransfer.2012.10.031.
29. Q. LI et al., “Development, Verification and Application of a New Model for Active Nucleation Site Density in Boiling Systems,” *Nucl. Eng. Des.*, **328**, 1 (2018); https://doi.org/10.1016/j.nucengdes.2017.12.027.
30. A. W. ADAMSON, *Physical Chemistry of Surfaces*, Wiley (1997).
31. “Thermohydraulic Relationships for Advanced Water Cooled Reactors,” TECDOC-1203, International Atomic Energy Agency (2001).
32. J. KIM, “Review of Nucleate Pool Boiling Bubble Heat Transfer Mechanisms,” *Int. J. Multiph. Flow*, **35**, *12*, 1067 (2009); https://doi.org/10.1016/j.ijmultiphaseflow.2009.07.008.
33. D. G. CAHILL et al., “Nanoscale Thermal Transport,” *J. Appl. Phys.*, **93**, *2*, 793 (2003); https://doi.org/10.1063/1.1524305.